



HAL
open science

Characterization of the oxidation of C/C/SiC composites by Xray micro-tomography

J. P. Goulmy, O. Caty, F. Rebillat

► **To cite this version:**

J. P. Goulmy, O. Caty, F. Rebillat. Characterization of the oxidation of C/C/SiC composites by Xray micro-tomography. *Journal of the European Ceramic Society*, 2020, 40 (15), pp.5120-5131. 10.1016/j.jeurceramsoc.2020.06.042 . hal-03294393

HAL Id: hal-03294393

<https://hal.science/hal-03294393>

Submitted on 22 Aug 2022

HAL is a multi-disciplinary open access archive for the deposit and dissemination of scientific research documents, whether they are published or not. The documents may come from teaching and research institutions in France or abroad, or from public or private research centers.

L'archive ouverte pluridisciplinaire **HAL**, est destinée au dépôt et à la diffusion de documents scientifiques de niveau recherche, publiés ou non, émanant des établissements d'enseignement et de recherche français ou étrangers, des laboratoires publics ou privés.



Distributed under a Creative Commons Attribution - NonCommercial 4.0 International License

Characterization of the oxidation of C/C/SiC composites by Xray micro-tomography

J.P. Goulmy¹, O. Caty¹, F. Rebillat¹

¹*Laboratoire des Composites Thermostructuraux,
University of Bordeaux et CNRS/SAFRAN/CEA
3 allée de la Boétie, 33600 Pessac, France*

Corresponding author :

goulmy@lcts.u-bordeaux.fr (J.-P. Goulmy)

(+33) 4 42 93 82 23

Abstract:

The objective of this paper is to determine the influence of the nature of the C/C/SiC composite on the oxidation rate of fibers and the interphase and the development of oxidation pathways using characterization techniques such as Xray micro-tomography (μ CT), scanning electron microscope (SEM) and optical microscopy (OM). The microstructure of two C/C/SiC composites (named 2D-RMI and 2D-CVI) was characterized before and after ageing tests performed by Thermogravimetric Analysis (TGA) under dry air at 1000°C and 1300°C. The three techniques are complementary and tomography appears to be a promising means for monitoring the oxidation of parts in service. Moreover, the oxidation of a fiber does not develop in a parallel plan to the section but as conical shape. To calculate the oxidation kinetics related to the surface, it is therefore necessary to take into account the geometry of the fibers that offers a much more important reactive surface.

Keywords: CMC; C/C/SiC; Tomography; TGA; Oxidation; Tomography

1. Introduction

C/C/SiC composites are used in many fields of application, such as brake discs for the automotive industry, satellite structure manufacturing, aeronautics and aerospace for rocket nozzle manufacturing or as re-entry thermal protection shields for space vehicles [1]–[5]. These materials have the required mechanical properties, particularly at high temperatures [6]. However, oxidation is expected in the severe environments of applications. Thus, the deposition of a coating on the surface of the composite is required [7]–[12].

Due to the varied applications, the mechanical and microstructural properties of C/C/SiC materials are diverse and depend mainly on the components used but also on the types of processes chosen to carry them out (Chemical Vapor Infiltration (CVI), Reactive Melt Infiltration (RMI), Polymer Infiltration and Pyrolysis (PIP)). The chemical composition, the quantity and the size of the pores, the fibrous architecture and the nature of fibers are some of the elements that can have an impact on the oxidation of these materials [13]–[15]. Micro-cracks are typically observed into C/C/SiC materials and are related to the significant thermal expansion mismatch between the fibers and the matrix [6], [16], [17]. Oxygen can then penetrate into the composite through these cracks and generate catastrophic degradation of the material under certain conditions [8], [18]. A good knowledge of oxidation mechanisms and kinetics for different kinds of C/C/SiC materials is then necessary to ensure their mechanical resistance at temperatures above 1000°C [7], [18]–[21]. It has been shown by many authors that surface reaction rates depend on the type of carbon, inducing selective surface attacks. Oxidation is preferably carried out along the fiber axis at the fiber/matrix interface [22]. In addition, more ordered graphitic carbon is less sensitive to oxidation [23], [24]. The fibers derived from polyacrylonitrile polymers (PAN) being more crystalline inside than at the edges, oxidation is promoted at the edges [24]. The fiber shape becomes conical once oxidized [25].

To characterize the oxidation kinetics of these composites, TGA (ThermoGravimetric Analysis) is the most widely used method in the literature with a follow-up of the evolution of the mass of the sample as a function of time [7], [9], [26]. Characterizations by optical and scanning electron microscopies are generally carried out to evaluate the impact of oxidation on the microstructure of materials. However, in recent years, the practices to observe microstructure have gradually changed with the development of non-destructive techniques such as tomography. This technique has already been used by few authors to characterize the microstructure of C/C/SiC composites during mechanical tests [27], [28], between different stages of the manufacturing process [29], [30] or after oxidation of the material [31]. For the time being, the authors have been satisfied with qualitative

characterizations, but this characterization technique allows to evaluate in a more quantitative way the quantity of consumed carbon during different heat treatments. In the future, monitoring the oxidation development into these materials should be achievable under simultaneous loading, for example.

The objective of this paper is to characterize and compare the oxidation of two C/C/SiC composites developed from different processing methods (RMI and CVI) and having different fibrous architectures. For this purpose, the contribution of various characterization techniques such as TGA, ex-situ Xray micro-tomography (μ CT), optical microscopy (OM) and scanning electron microscopy (SEM) is discussed. This paper is organized as follows. In the first section, the two materials and methods are introduced. In the second section, obtained results on both, non-oxidized and oxidized materials, are presented. Then, the achieved results by tomography are compared with those from other characterization methods. Finally, a discussion is proposed to evaluate the ability of tomography to characterize the oxidation into these two materials.

2. Materials and methods

The materials used in this study are C/C/SiC fiber-reinforced matrix composites produced by SGL and MT Aerospace. The SGL material, later named 2D-RMI, has a matrix processed by Reactive Melt Infiltration (RMI), while the composites from MTA (2D-CVI) were developed by Chemical Vapor Infiltration (CVI). The architecture of the two composites is distinct. The 2D-RMI material has a 2D woven structure with 13 plies of type [0,90]. The 2D-CVI material is a laminated woven composite fabric with 23 plies oriented at 0°/90° and +45°/-45°. More details regarding the manufacturing processes used to get these composites are available in reference [3].

Conventional techniques were used to characterize the microstructure characteristics of the two composites and to provide a reference viewpoint for discussing the analyses performed using μ CT. The global porosity ratio of composites is deduced from the density values evaluated by combining water and helium porosity techniques. The microstructures and the morphologies of composites were examined with a scanning electron microscope (SEM, FEI 400 FEG). Polarized light microscopy analyses are performed to determine whether composites contain pyrocarbon and to evaluate the nature and the thickness of the pyrocarbon. The study was performed with an optical microscope Nikon ME500L working in reflection mode. This microscope is equipped with a HD CCD camera with digital output. The CCD camera (Nikon Digital Camera DMX 1200) converts linearly the intensity into

an 8-bit grayscale value. The microscope is also equipped with graduated polarizer and analyzer. The method for recording the images and analyzing them has been detailed previously in the following reference [32].

The method of mercury porosimetry (Autopore IV, Micromeritics) was used to determine the pore size distribution. Before intruding mercury in step-wise pressure increments in the range from 0.0021 MPa to 34.4 MPa, the composites were oven-dried at 105 °C and vacuum degassed. The measurements were done in two replicates for each composite. Pore size distribution was determined using the Washburn equation [33] :

$$P = \frac{2 \gamma_{Hg} \cos\theta}{r} \quad \text{Eq. 1}$$

Where γ_{Hg} is the surface tension of mercury (0.485 J m⁻²), θ is the contact angle of mercury (130°), P is the external pressure (Pa) applied in the vacuum chamber, and r is the radius of pore aperture (m) for a cylindrical pore. Average pore radius was obtained by assuming that all pores are right cylinders. Thus, when the volume ($V = \pi r^2 L$) is divided by the pore area ($A = 2\pi r L$), the average pore radius r is equal to $2V/A$.

Micrographs supply only 2D surface data. To obtain information on the oxidation kinetics inside samples it is possible to cut and image the specimen. Unfortunately, this operation is long and destructive. To obtain non-destructive tridimensional (3D) and inside samples data, X-ray micro-computed tomography (μ CT) is particularly efficient [34], [35]. At the laboratory, resolution of a few microns is reachable [36]. μ CT presented in this paper were acquired on a VTomX-S (GE) system with the 180 keV nanofocus XRay tube. Resolution of images was set to 4 μ m and 8 μ m to be enough resolved to observe voids and matrix consumption during oxidation tests and enough high to have a representative volume to be studied (sensor 2024x2024 pixels). To get a resolution at 4 μ m, acquisition parameters were : tension 130 keV, intensity 250 μ A, opening mode 0, no filter, exposure time 500 ms, averaging 3 and 2500 images for 360°. At 8 μ m, these parameters become : tension 140 keV, intensity 250 μ A, opening mode 0, no filter, exposure time 500 ms, averaging 3 and 2500 images for 360°. Scan durations is about 1h. For all samples an initial state and five oxidation states were acquired (after 15 min, 60 min and 180 min of oxidation test at 1000°C and after 15 min and 30 min at 1300°C - see the end of this section for details). Analyzed volumes are all larger than 350 μ m³, respectively 351 μ m³ for the 2D-RMI and 506 μ m³ for the 2D-CVI sample.

The SiC matrix and pores were segmented by greyscale thresholding using the Avizo® software [37]. Once the different phases are separated, an analysis of the pore distribution is carried out. Two processes on the images are performed: an opening to remove the noise, and a separation to

distinguish the particles from each other. Because values of equivalent diameter can be calculated from several viewpoints depending on the shape of the pores, a pore sphericity φ calculation is performed as follows:

$$\varphi = \frac{\text{surface of the sphere of the same volume as the pore}}{\text{pore surface area}} \quad \text{Eq. 2}$$

In other words, it means :

$$\varphi = \frac{\pi^{1/3} (6 \text{ Volume}3d)^{2/3}}{\text{Area}3d} \quad \text{Eq. 3}$$

Where *Volume3d* and *Area3d* are the volume and the area of the pore calculated by Aviso® software [37].

Finally, ThermoGravimetric analyses (TGA) of C/C/SiC composites were conducted in order to investigate their oxidation behavior. The TGA apparatus used is a Setsys 1600 vertical furnace from Setaram. During tests, samples are placed in an alumina basket. All samples have a SiC seal coating except on one surface to get an access to all constituents from one single, well defined, surface (Figure 1). The uncoated surface is polished and its surface area depends on the studied material ($S_u(2D-RMI) = 0.36 \text{ cm}^2$, $S_u(2D-CVI) = 0.23 \text{ cm}^2$). The tests are performed at two distinct temperatures: 1000°C and 1300°C with holding times ranging from 15 minutes to 180 minutes under dry air environment. During the rise and decrease in temperature, the samples were placed under argon flow to limit oxidation of the materials. Using the mass evolution curves as a function of time, it was possible to extract the oxidation kinetics of the various samples. For each condition and each material, the oxidation rate is determined at 50% of the mass evolution curve. This mass lost rate is reported to the uncoated free surface of the sample to get $k_{\text{Suncoated}}$.

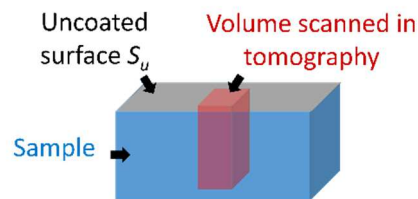


Figure 1. Sample used for TGA measurements.

3. Results

3.1 Characterization of non-oxidized materials

3.1.1 Classical measurements characterization

A summary of the observations and the measurements made using conventional characterization tools is presented in Table 1. The measured bulk density for 2D-RMI material is 1.89 ± 0.02 compared to 2.00 ± 0.01 for true density. The porosity is estimated to 6 ± 1 %. This value is slightly higher than the characteristic data of RMI materials [3], [15]. The 2D-CVI material has a bulk density of 2.06 ± 0.02 , a true density of 2.41 ± 0.02 and a porosity of 14 ± 1 %. These values are in agreement with the observations made in the literature regarding the materials developed by CVI [3], [15]. The 2D-RMI material contains around 5% of free silicon (in white on the left figure of Table 1) and approximately 15 % of residual carbon matrix. For comparison, the material developed by CVI does not have any of both.

Figure 2 compares polarized light microscopy analyses performed on the two materials. A colored ring around the fibers, characteristic of pyrocarbon, is observed. The extinction angle, linked to the structural organization of pyrocarbon, was evaluated for each material. Pyrocarbon is smooth laminar in nature for the 2D-RMI and dark laminar type for the 2D-CVI material. This latter is therefore of lower quality than inside 2D-RMI material [38]. The average thicknesses of pyrocarbon are close to $0.5 \mu\text{m}$ for both materials.

SIGRAFIL fibers and Ex PAN fibers have been used to manufacture the 2D-RMI and 2D-CVI materials respectively (information provided by manufacturers). The average diameter of both kinds of fibers is about $7 \mu\text{m}$. Also, polarized light microscopy makes possible to highlight the differences in microstructure within the fibers since a ring with a diameter of about $3 \mu\text{m}$ is observed within each fiber (used either in 2D-CVI or 2D-RMI materials).

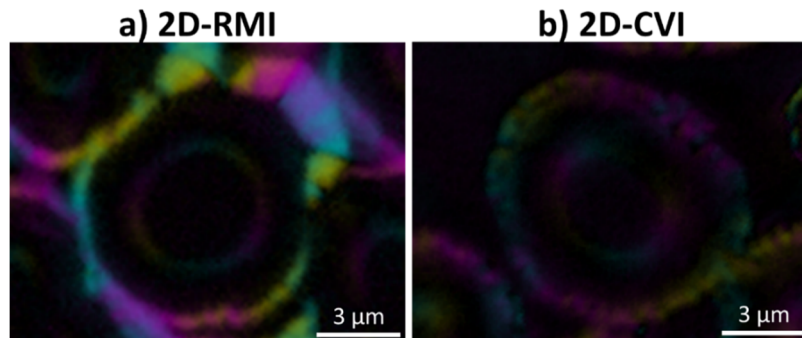


Figure 2. Comparisons of polarized light images of the two materials.

Different morphologies of cracks were observed by optical microscopy. Microcracks are related to the significant thermal expansion mismatch that exists between the fibers and the matrix. Despite the presence of the pyrocarbon interphase that may act as a buffer layer, the matrix still encountered both axial and radial tensile residual stresses upon cooling from the processing temperature, resulting in microcracking [6], [16]. The majority of cracks are perpendicular to the fibers (materialized by red arrows on the images in table 1), inside each fiber bundle as well as through the surrounding C and SiC matrix. These cracks appear to be homogeneously distributed with an average spacing of around 75 μm and they are largely opened when located inside the bundles. However, their width stays lower than 2 μm .

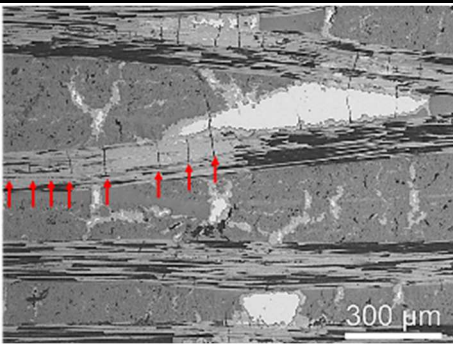
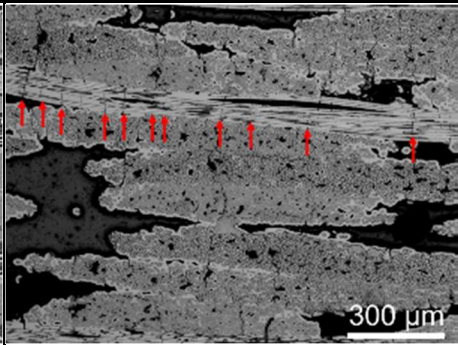
Name	2D-RMI	2D-CVI
Microstructure as received (optical microscopy) (red arrow = intra-wire cracks)		
Manufacturing process	RMI	CVI
Fiber architecture	2D woven	2D woven laminate
Porosity (%)	6 ± 1	14 ± 1
Bulk density ($\text{g}\cdot\text{cm}^{-3}$)	1.89 ± 0.02	2.06 ± 0.02
True density ($\text{g}\cdot\text{cm}^{-3}$)	2.00 ± 0.01	2.41 ± 0.02
Fiber size (μm)	7 ± 0.5	7 ± 0.5
Nature of the fibres	SIGRASIC®	Ex-PAN
Pyrocarbon thickness	$\sim 0.5 \mu\text{m}$	$\sim 0.5 \mu\text{m}$
Cracking density (wires)	1 crack / 75 μm	1 crack / 75 μm
Supplier	SGL	MT Aerospace

Table 1. Summary table of the microstructural properties of the two C/SiC composites: 2D-RMI and 2D-CVI.

Figure 3 shows the pore distribution obtained using mercury porosimetry for the two materials a) 2D-RMI, and c) 2D-CVI. Measurements were made on two samples for each material. For 2D-RMI material, measurements are repeatable. Three populations are observable, with an average diameter of 0.3 μm , 80 μm , and 250 μm . Concerning the 2D-CVI material, two pore populations are visible with an average diameter of 0.7 μm and 30 μm .

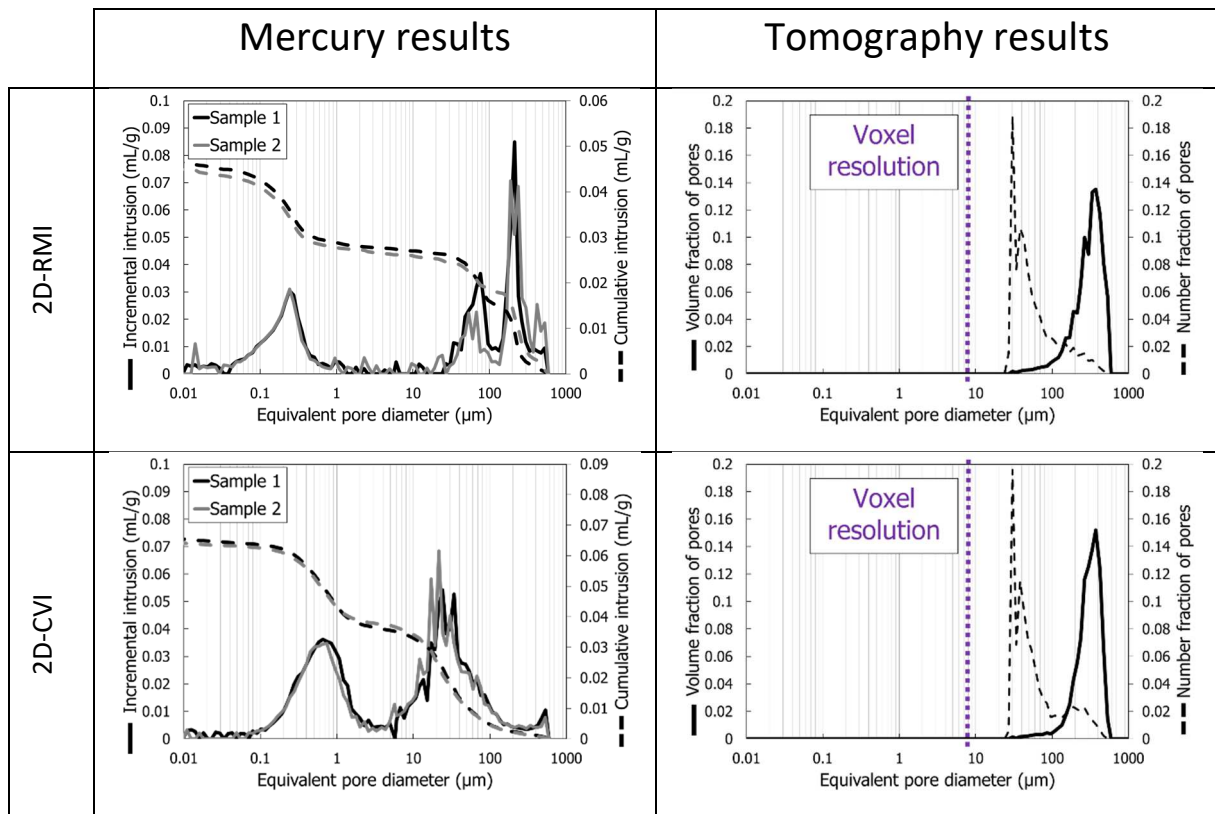


Figure 3. In left, results from the mercury porosimetry; incremental intrusion pore (straight lines) and cumulative intrusion (dot lines) versus equivalent pore diameter for the two composites. In right, results from tomography images, volume fraction of pore (straight lines) and number fraction of pores (dot lines); versus equivalent pore diameter for the two composites (voxel resolution = 8 μm).

3.1.2 Tomography characterization

Tomography was performed with a resolution of 8 μm on non-oxidized samples. The images obtained at different magnifications are gathered in Table 2. They show that the use of a resolution of 8 μm allows a qualitative overview of the two composites with a high quality since the pores, fibers and SiC matrix seem clearly distinguishable. The typical grayscale histograms obtained for the two composites are presented in Table 2. It appears that the gray scale difference between the carbon fibers and the pores is sufficient to separate and quantify the porosity of the materials. Thus, the treatment of images is applied as previously described in section II to segment pores in the material.

Figure 4 shows the sphericity coefficient of pores distribution for the two composites, calculated from Eq. 2. Although the major geometric characteristic of pores is located around a sphericity value

equal to 1, all pores cannot be considered as spheres. It has to be notice that the distribution in terms of sphericity is very similar for the two composites.

Thus, it was decided to calculate the equivalent diameters *EqDiameter* according to the Eq. 4 where *Volume3d* is the volume of the pore.

$$EqDiameter = \sqrt[3]{\frac{6 Volume3d}{\pi}} \quad \text{Eq. 4}$$

The pore distribution obtained in tomography is shown in Figure 3 for the two materials: c) 2D-RMI, and d) 2D-CVI (on Figure 3, the intervals of measurements are similar whatever the method used to quantify the porosity distribution). Volume fraction of pores and number fraction of pores are displayed in straight line and dot line respectively. The distributions of pore sizes are similar for the two materials. Two populations can be separated (in number): one of less than 100 μm in diameter and another more than 100 μm .

On the other hand, it is not obvious to define thresholds to quantify all the phases in these materials. For example, it is unlikely to determine the amount of carbon fibers and SiC matrix in 2D-CVI samples. Also, while there are four phases in the 2D-RMI composite (porosity, carbon, SiC and free Si), only three phases are discernible on the grey scale histogram, the dissociation between SiC and free Si being not possible. A dissolution of the Si phase as proposed by Wan et al. could be performed to distinguish the Si and SiC phases [30].

A comparison of the results obtained between the two characterization methods (tomography and mercury porosity) is proposed in detail in section 4.1.

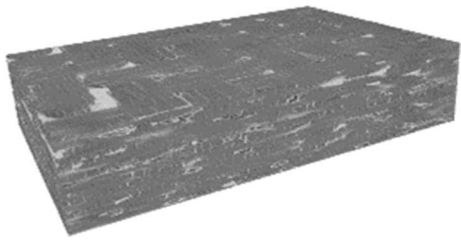
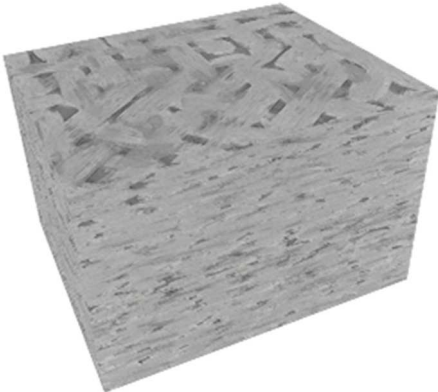



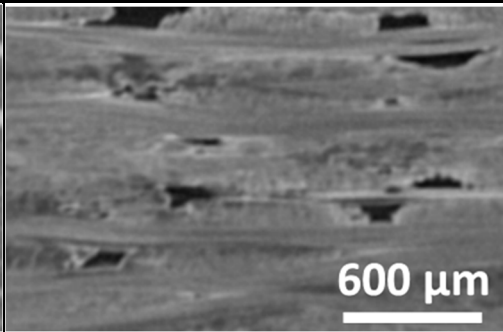
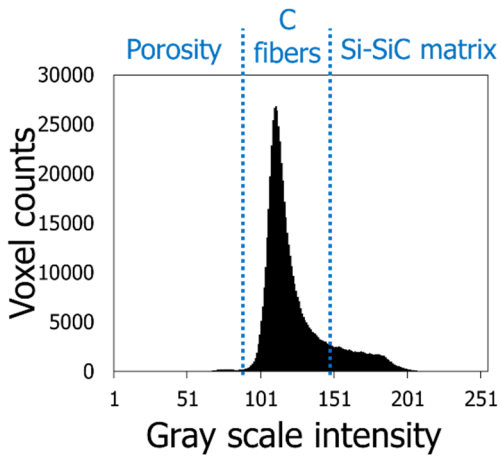
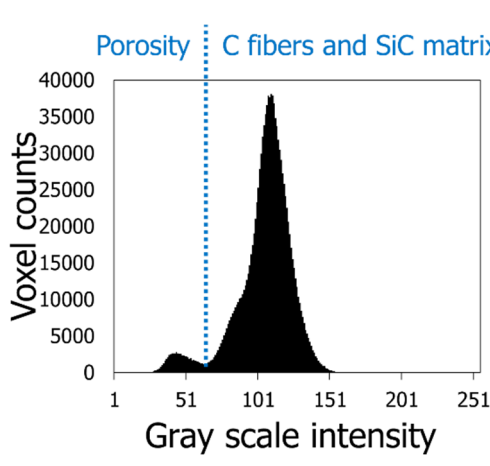
Name	2D-RMI	2D-CVI
Whole Tomography (voxel resolution = 8 μm)		
Zoom in the sample (2.7 mm ³) (voxel resolution = 8 μm)		
Surface (voxel resolution = 8 μm)		
Grayscale histogram	 <p>Porosity C fibers Si-SiC matrix</p> <p>Voxel counts</p> <p>Gray scale intensity</p>	 <p>Porosity C fibers and SiC matrix</p> <p>Voxel counts</p> <p>Gray scale intensity</p>

Table 2. Tomography of the microstructures as received at a resolution of 8 μm : 3D visualization and typical histogram of grey levels obtained for the two materials.

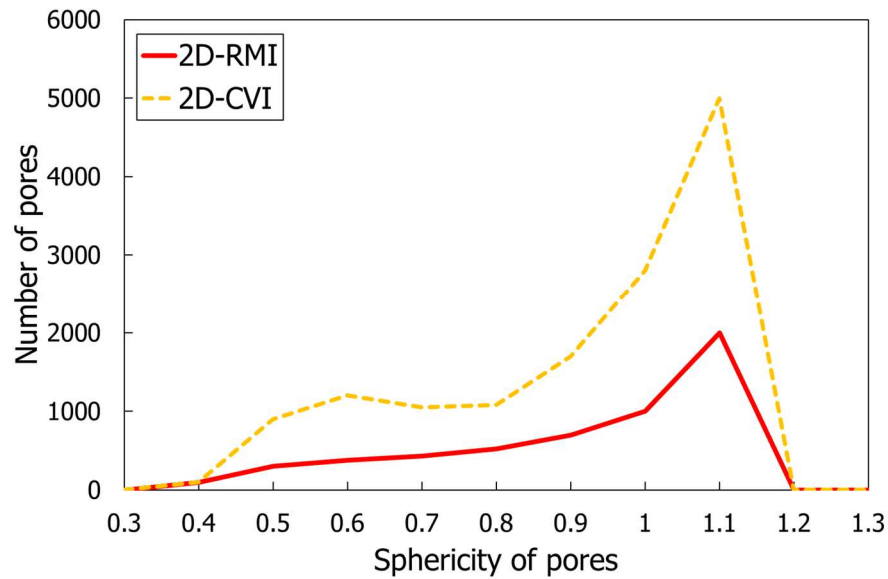


Figure 4. Sphericity of pores distribution for the two composites obtained by tomography analyses.

3.2 Characterization of oxidized materials

3.2.1 Oxidation kinetics of composites

Figure 5 shows the evolution of the loss mass related to the uncoated section S_u as a function of time and Figure 6 presents a comparison between the oxidation kinetics calculated for the two composites at 1000°C and 1300°C and the values obtained in the literature on ex-pan and cellulose fibers under the same environmental conditions [39]. A parabolic behavior of the evolution of mass loss is obtained for the longest holding times. The tests appear repeatable for the same material since the registered weight loss for the different holding times are identical on the same durations. As expected, an increase in oxidation kinetics is obtained with a rise in temperature. However, the oxidation kinetics do not seem to evolve in the same way for the two composites. This evolution is lower for the 2D-RMI material between 1000°C and 1300°C. Finally, compared to the previously obtained results on ex-pan or ex-cellulose fibers, the oxidation kinetics obtained in these studies are ten to one hundred order higher [39]. This scatter will be later discussed in regard to the developed oxidized surfaces.

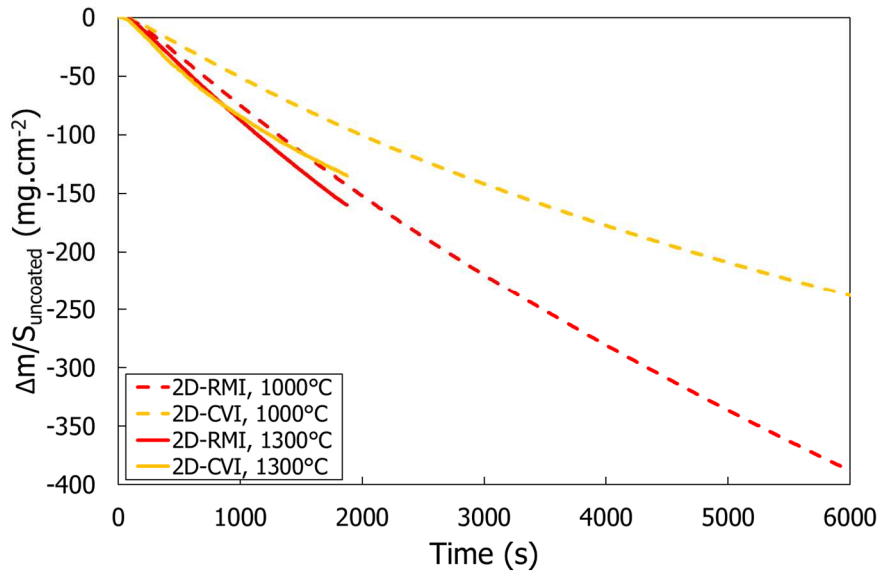


Figure 5. Evolution of the weight loss related to the uncoated section S_u , as a function of time.

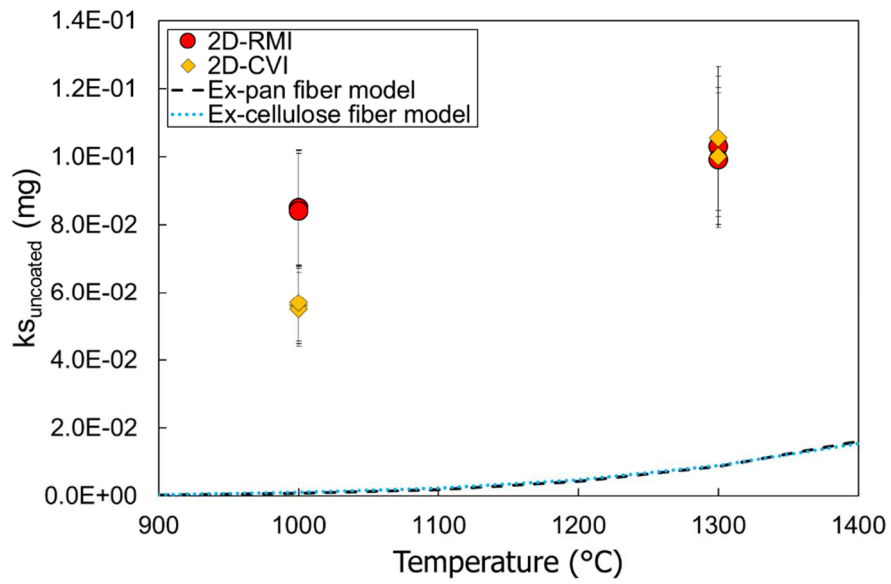


Figure 6. Comparison of composite oxidation kinetics with an ex-pan and cellulose fiber model [39].

3.2.2 Microstructural observations

3.2.2.1 Surface characterization

Figure 7 shows typical examples of developed oxidized surfaces on the two composites, obtained using SEM. The oxidation appears relatively homogeneous over the whole section. For a similar duration (15 minutes) at 1000°C and 1300°C, the oxidized surfaces are similar. From an outside observation viewpoint, this remark remains true for the largest investigated holding times (180 minutes at 1000°C and 30 minutes at 1300°C).

For the two materials, the main oxidized constituents are both carbon fibers and pyrocarbon coating around them. For the 2D-CVI material, oxidation mainly propagates where fibers are oriented perpendicular to the free surface of the composites. Longitudinal fibers are also affected by oxidation but their oxidation seems to be less extended. For the 2D-RMI material, the oxidized surfaces appear more "disturbed" because of fibers initially oriented in many directions. The observed macroscopic pores could be related to the initial presence of free carbon blocks in the matrix, coming from the manufacturing process.

Moreover, a layer of SiO₂ is observed on the surface of 2D-RMI samples at 1300°C after 30 minutes of ageing (Figure 8). This glassy phase is distributed over a large part of the composite surface and extends with the holding time. Further, the fibers under the glassy phase are oxidized, suggesting that this oxide scale was created before oxidation of fibers since fibers extremities have left prints, visible on the micrographs (Figure 8). During polishing, very few silicon coming from the RMI matrix can be spread over all the surface and lead to this extremely thin silica scale, just after the departure of the oxidation test.

Figure 9 allows comparing surface images obtained by optical microscopy (a, b) and tomography (c, d) for the two materials: 2D-RMI (a,c) and 2D-CVI (b,d). All oxidized areas appear black with the release of carbon on any images. Since the amount of SiC around the fibers inside 2D-RMI material is extremely small, compared to the 2D-CVI material, black surfaces are highly extended on optical microscopy images on this first one. Reversely, for the 2D-CVI material since the amount of SiC is higher around the fibers, only the initial position of fibers appears in black. Respectively, differences should be found on images obtained in tomography, even if the resolution used to observed oxidized samples is 4 μm/voxel, compared to 0.68μm/pixel for optical microscopy analyses. The presence of SiC in large quantities around the fibers is seen through the change of the grey levels (for 2D-CVI material) (Figure 9).

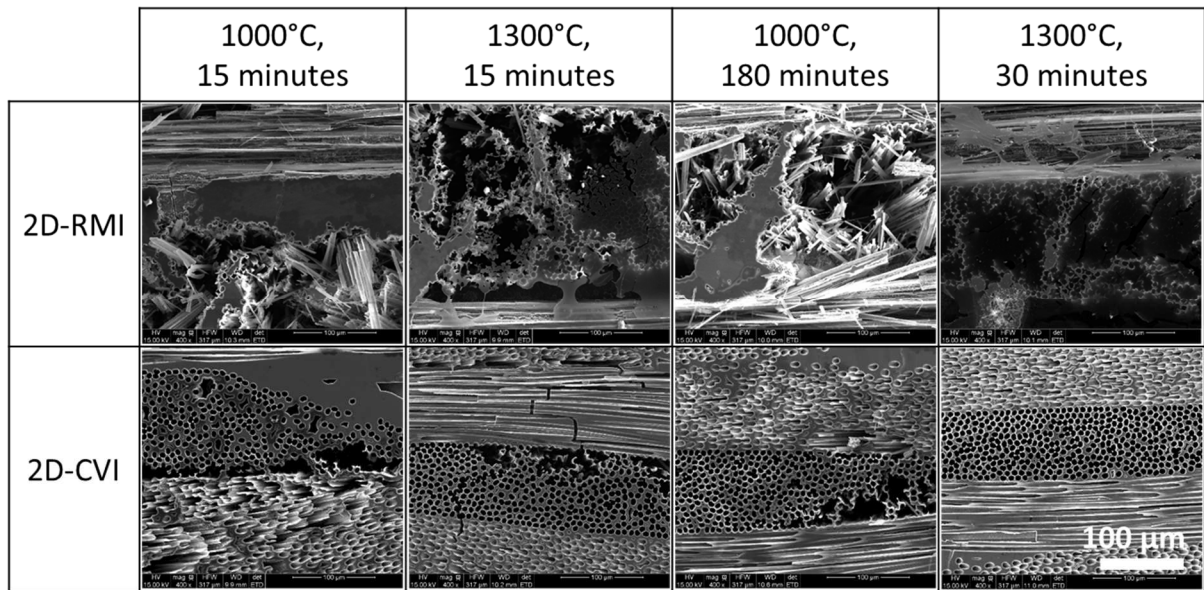


Figure 7. Developed oxidized surfaces obtained after thermal treatments at 1000 and 1300°C, SEM images obtained in secondary electrons.

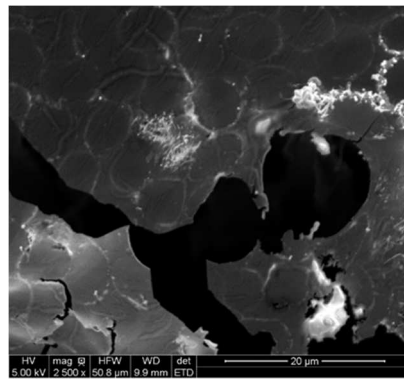


Figure 8. SEM micrograph of the surface of and 2D-RMI sample covered by a SiO_2 glass phase after treatment at 30 minutes at 1300°C.

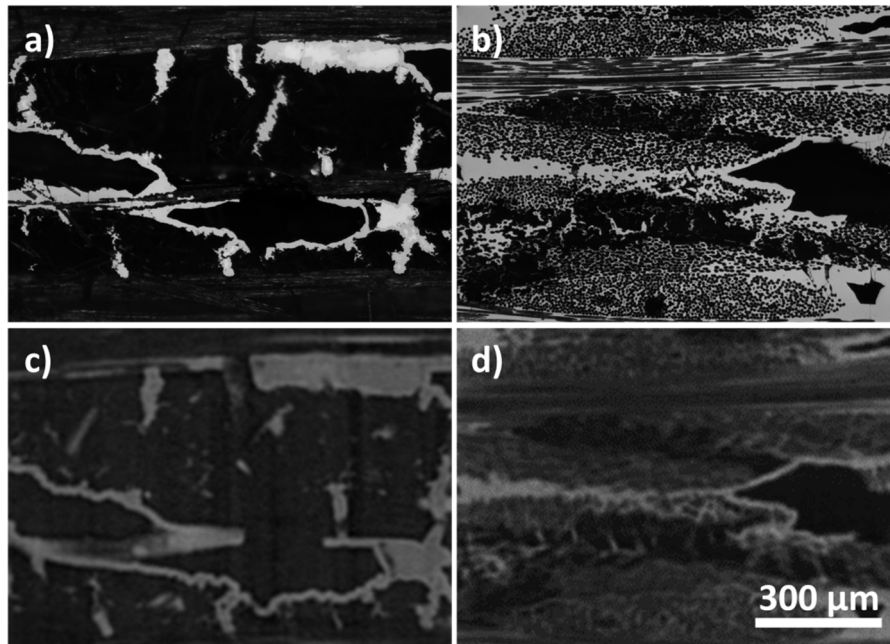


Figure 9. Comparison of the resolution obtained by optical microscopy (a,b) and tomography (c,d) for the two materials 2D-RMI (a,c) and 2D-CVI (b,d).

3.2.2.1 *In-depth characterization*

The successive observations in optical microscopy of polished surfaces of the oxidized samples allow accessing to the position of the oxidation front and to its propagation in depth in function of holding time in ageing conditions. Figure 10 shows such observations of samples aged at 1300°C for 15 minutes, a) 2D-RMI and b) 2D-CVI, (the uncoated surface is located at the bottom of the images). The oxidized zones again appear in black. They preferentially follow the position of fibers oriented at 90° and 45° with respect to the uncoated surface. Moreover, the oxidation of fibers oriented at 0° is more pronounced for the 2D-RMI material than for the material processed by CVI. No other oxidation zones were observable outside this area.

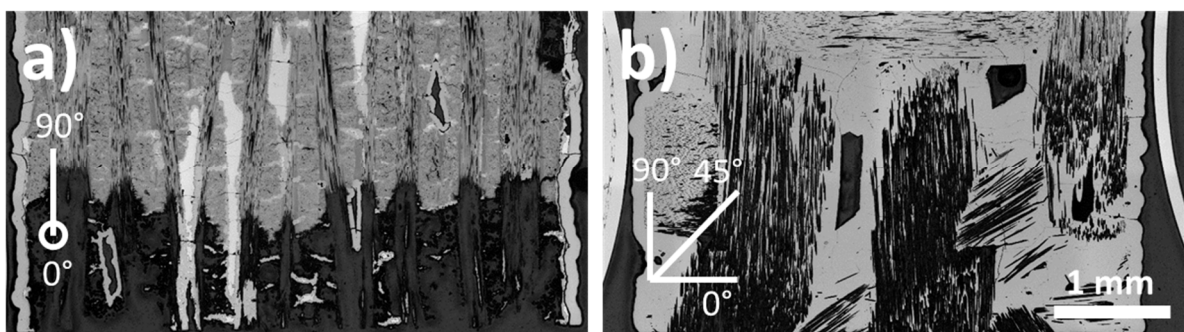


Figure 10. Observations by optical microscopy of samples aged at 1300°C for 15 minutes, a) 2D-RMI and b) 2D-CVI, (The uncoated is located at the bottom of images).

As shown on optical micrographs of Figure 10, the oxidation front is not planar. Optical micrographs supply only 2D information. To analyze the whole oxidation front, 3D images are necessary. X-Ray micro-tomography, appears then to be well fitted to follow the propagation of the oxidation for different oxidation times, to analyze the morphology of the front in depth and in 3D and to extract more accurate oxidation kinetic laws.

As before, for reasons of acquisition time, it is impossible to visualize the entire volume of samples in a same run by keeping a resolution less than 4 μm . The hypothesis of homogeneity of microstructure and oxidation is therefore realized. This seems consistent in view of the observations made by optical microscopy that show homogeneous oxidized surface of the samples. The volumes analyzed are bigger than 22.4 mm^3 for all samples. Figure 11 shows the tomography images of both composites aged at 1300°C for 15 minutes under dry air in TGA. The oxidation front is relatively well defined for 2D-RMI material, while this inside a 2D-CVI material is more blurred and irregular.

Figure 11 presents an image (obtained by tomography) taken perpendicular to the uncoated surface of the 2D-RMI material aged at 1000°C for 15 minutes. This figure shows significant differences between the oxidation areas in depth inside the composite. However, to extract the position of the oxidation front (Figure 12), a manual thresholding (by indexing) is necessary to dissociate the initial porosities from the oxidized zones; their respective grey levels on pictures are comparable. As previously observed, on the surface of the composite (0 μm), the fibers are fully oxidized. At a depth of 900 μm , only a few areas are oxidized, corresponding to the fibers oriented perpendicularly to the uncoated surface; the fibers oriented parallel to the surface do not appear oxidized (0° on Figure 10). At 1800 μm , no fiber is oxidized.

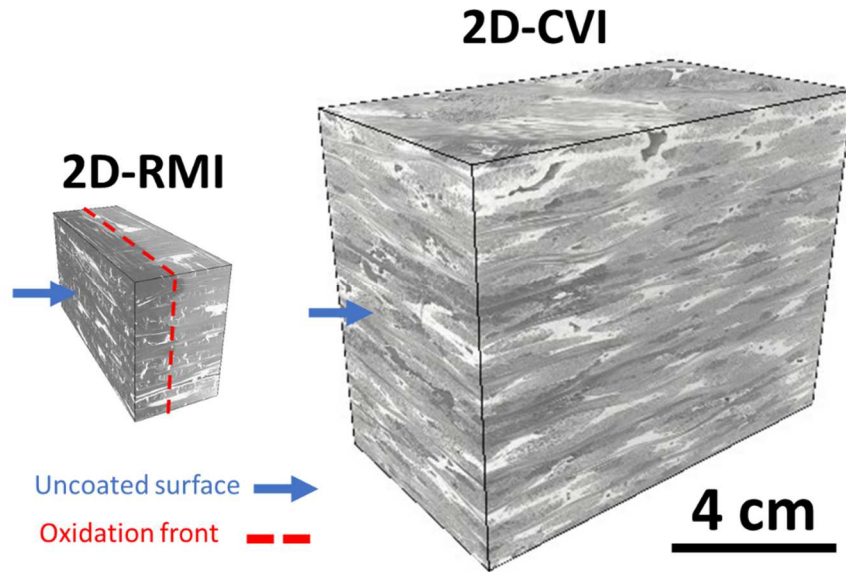


Figure 11. Tomography images of both composites after an ageing treatment at 1300°C for 15 minutes in dry air.

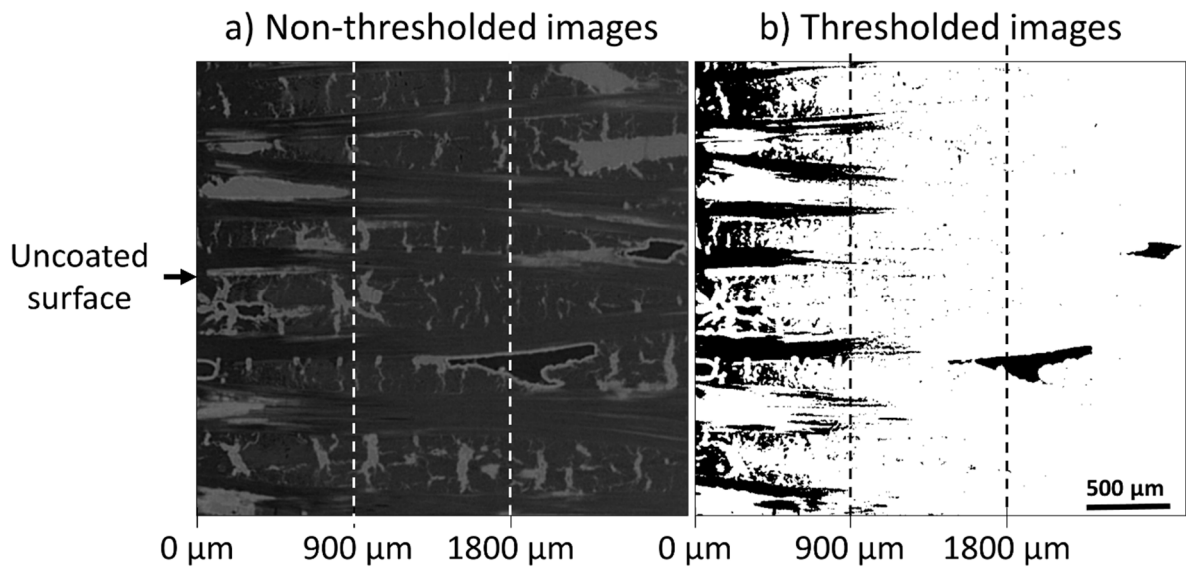


Figure 12. Processing carried out on images obtained by tomography on a 2D-RMI sample after ageing treatment at 1000°C for 15 minutes in dry air; a) Non-thresholded image, b) thresholded image (in black, porosity and oxidized carbon).

4. Discussions

4.1 *Characterization of non-oxidized materials*

An analysis of open pore distribution using the mercury porosimetry measurement shows the presence of: micropores smaller than 10 μm , mesopores (between 10 and 100 μm) and the macropores larger than 100 μm . At the same time, tomography highlights a majority population with average equivalent diameters between 10 and 100 μm and a minority population with an average equivalent diameter larger than 100 μm . Two common populations are therefore obtained using the two characterization techniques: mean equivalent diameter 50 μm and larger than 100 μm which could correspond to the mesoscopic and macroscopic pores inside the composites. However, between these both techniques, the different methods to evaluate the radius certainly induce a scatter on the values of mean equivalent diameters. Starting from the volume of a pore, its diameter is either that of an equivalent sphere (Eq. 4) (tomography) or that of the entrance of a cylinder (mercury porosimetry). Of course, the mean values extracted from tomography should be always higher than those from mercury porosimetry. The right values are certainly between, according to the sphericity coefficient (Eq. 2). At least, the values of the whole volume of pores (or porosity ratio) are close between the both used methods of measurement. Finally, the average pore radius r extracted from mercury porosity should often be a default value, hence the need to consider a percentage of porosity in the comparison, values that can be extracted from each technique.

From these same images obtained by tomography, it is feasible to evaluate the volume fraction of constituents. Using the previous values of porosity fraction, another calculation method of the true density becomes available. This latter value can be compared to conventional density measurements (Table 1). The theoretical densities of SiC matrix, free Si and carbon fiber are taken as 3.2 $\text{g}\cdot\text{cm}^{-3}$, 2.8 $\text{g}\cdot\text{cm}^{-3}$ and 1.8 $\text{g}\cdot\text{cm}^{-3}$ respectively. Since free silicon and SiC are not separable, an average density value of 3 $\text{g}\cdot\text{cm}^{-3}$ is kept in the calculation about the 2D-RMI composite.

The amount of SiC (or Si-SiC for 2D-RMI material) seems well defined since the difference between the measured densities by conventional methods and calculated ones from tomography is less than 12% for 2D-RMI material.

Table 3 shows the pore repartitions extracted from image analysis within the two composites. Due to the resolution used here (8 μm), the smallest pore diameter detectable in tomography is greater than 8 μm . These pores can be classified in function of their sizes, described through an equivalent diameter (Eq. 2): less than 100 μm (mesopores) (which corresponds to the majority

population by number) and more than 100 μm (macropores). The part of smallest pores (equivalent diameters less than 100 μm) is homogeneously located within the composites while the part of biggest pores (with a size greater than 100 μm) is detected at the intersection between the bundles. Each pore is differently colored as soon as a pore is not connected to the others pores, close neighboring (Table 3). Due to the high number of plies contained in the 2D-CVI composite, this population of macroscopic pores is particularly large.

It has to be noticed that all these closed pores are not directly accessible by mercury porosimetry but their fraction is only deduced from the difference between the true and buck densities. Consequently, the presence of open pores larger than 100 μm observed in mercury porosimetry on 2D-RMI material is certainly related to the probability to find large pores connected to the surface, along the cut surfaces.

However, at least 50% of the pores contained in the composites have a size below 8 μm , according to the mercury porosimetry measurements (Figure 3). It is therefore consistent to observe a difference of more than 50% between the tomography and conventional methods concerning the porosity values (Table 3). The calculation from images at a resolution of 4 μm on the 2D-RMI material give a porosity of about 4%. By increasing the accuracy of images, the relative gap with conventional methods is reduced to 33.6%. Under the same conditions, no significant influence was obtained on the amount of SiC (19.3% versus 19.5% with a resolution of 4 μm and 8 μm respectively). Moreover, this observation is in accordance with results from [29] when measurements are carried out on a 2D-RMI equivalent material, using a resolution of less than 2 μm ; in this conditions, a good agreement is gotten between mercury porosity and tomography measurements (without specifying the size of the pores measured by the mercury porosity technique). Thus, it may be necessary to use a much lower resolution to be able to fully describe the population of pores, up to those with an average equivalent diameter smaller than 0.9 μm . As the porosity is underestimated, the content of carbon fiber is therefore overestimated [3]. Despite these previous scatters, the final differences between values of true densities, calculated by these both approaches, remain very low, less than 5% (in calculation from tomography images, 2% vol. of the composite (50% of the whole porosity) is switched in carbon, with a relatively low density).

Tomography therefore accurate characterization of pores possible, but only with a size larger than the selected working resolution. In addition, more data than by Archimed method or by mercury intrusion porosimetry are gotten since it is possible to isolate the open and closed pores and to have information on their shapes, their numbers and their locations inside composites. It is

therefore possible to use this technique to easily visualize the distribution of pores from a mesoscopic to macroscopic scale within C/C/SiC composites.

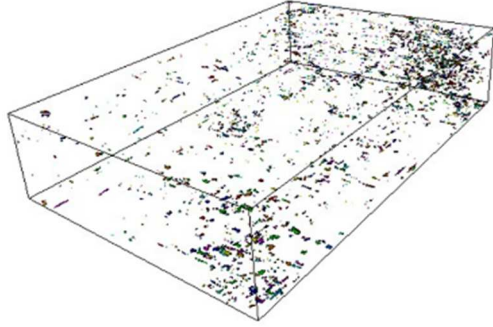
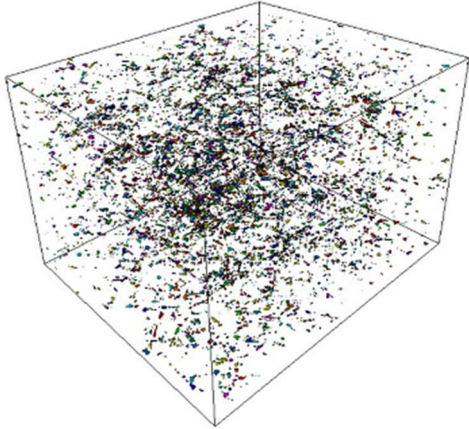
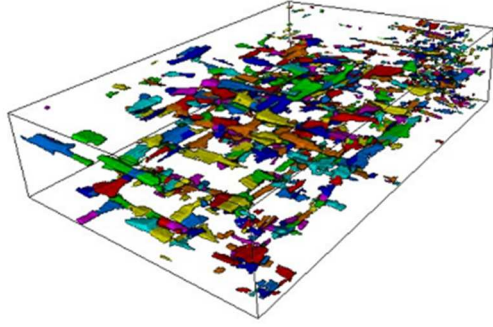
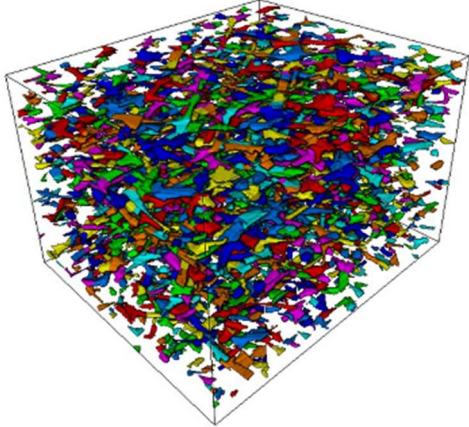
Name	2D-RMI	2D-CVI
Mesopores with an equivalent diameter < 100 μm		
Macropores with an equivalent diameter > 100 μm		

Table 3. Distribution of pores in the two composites from the tomography. For quantification, pores are labeled, colors correspond to pore labels.

Name	2D-RMI	2D-CVI
Content of carbon obtained by tomography (%)	92.9	-
Content of silicon carbide obtained by tomography (%)	5.4	-
Porosity obtained by tomography (%)	1.7	4.2
Porosity gap compared to a conventional method (%)	71.7	70
Density obtained by tomography (g/cm^3)	1.84	-
Density gap compared to a conventional method (%)	2.9	-
True density obtained by tomography (g/cm^3)	1.87	-
True density gap compared to a conventional method (%)	6.7	-

Table 4. Volume fractions and density values extracted from tomography images. Data not available for 2D-CVI material due to inability to clearly distinguish fibers and matrix with threshold image treatment.

4.2 Characterization of oxidized materials

Five highlights were identified through the analysis of TGA curves and microstructural observations done by OM, SEM and μ CT on oxidized materials:

- (i) The oxidation kinetics are of the same order of magnitude for the two composites but they are ten to one hundred order higher, compared to the oxidation kinetics on monolithic materials, mentioned in the literature [39].
- (ii) The increase of oxidation kinetics between 1000°C and 1300°C is lower for the 2D-RMI materials.
- (iii) A silica scale was observed on the surface of the samples of 2D-RMI material at 1300°C.
- (iv) The propagation fronts of oxidation are well defined within 2D-RMI materials while they are very difficult to observe inside 2D-CVI material by μ CT.
- (v) Oxidation takes place only on the surface and not into the bulk of the samples.

(i). The significant differences obtained between the oxidation kinetics of ex-pan fibers [39] and C/C/SiC composites in this study, indicates that the areas (S_u) considered for calculating the oxidation rates (k_{su}) should be highly underestimated. As mentioned before, it has been shown by many authors that surface reaction rates depend on the structure, the micro-texture and the chemical composition of carbon (hetero-atoms). These latter characteristics are known to induce selective surface attacks [19], [40]. For example, different oxidation rates, related to the crystalline organization of carbon, are reported between the carbon fibers and the pyrocarbon interphase [24], [41]. Thus, in the composite, the oxidation preferably occurs at the fiber/matrix interface along the fiber axis resulting in a conical shape of the tip of fibers, during oxidation [22]. Despite an oxidation leading to conical shaped fibers, the evolution of the mass loss over time can be nearly assimilated to a straight line during the first moments of tests under oxygen (Figure 5). Taking into account all these considerations, an oxidation scenario is proposed Figure 13:

- a) Initially, as the samples are uncoated on one face, after polished, all constituents over this reactive surface, the carbon fibers, the pyrocarbon interphase and the silicon carbide matrix are at the same height.
- b) After a few seconds under oxygen, according to its highest reactivity, the fibers are oxidized first. Later, oxidation of the fibers occurs preferentially on their outsides, generating

a "debonding length" (l_d) and inducing an increase of the reactive area against oxygen S_{ox} (green in the Figure 13).

c) The oxidation of the pyrocarbon interphase and carbon fibers continues until the increase of the debonding length allows developing a large reactive surface for the pyrocarbon up to present logically a similar global kinetics to that of the fibers. The reactive surface of the interphase, S_{ox} , then reaches a maximum value. A balance between the supply of oxygen and its consumption is reached. However, with the progression of the oxidation front deep inside the composite, the supply of oxygen can become limited by diffusion. A low decrease of the kinetic is then obtained.

d) After several minutes, the fibers and pyrocarbon continue to oxidize with a debonding length remaining constant. Observations at shorter times than those investigated (interrupted tests) or in-situ tests could be undertaken to confirm this scenario.

This scenario leads to writing, equations Eq. 5 to Eq. 8 when the time is long enough to get a constant oxidized surface (Figure 13.c). As the volume fraction of the carbon interphase is much smaller than that of the fibers, it can be assumed that the oxidation rate of the fibers and pyrocarbon are similar, in a first approximation to make easier the calculation (a debonding length at the fiber/matrix interface cannot be generated by the oxidation of the interphase). Based on the evolution of the global mass loss as a function of time, the oxidation rate (k) of the composite can be determined. Assuming that the recorded mass loss is essentially related to the oxidation of carbon fibers and pyrocarbon, the low mass gain generated by the creation of silica can be neglected. The extraction of k is done as following:

$$k = k_f S_{ox} \quad \text{Eq. 5}$$

Where k_f is the oxidation rate of the fibers defined by Zancanaro et al. at 1000°C and 1300°C [19], [39].

The open reactive surface against air is defined as :

$$S_{ox} = (s_i + s_f) \%S_f S_u \quad \text{Eq. 6}$$

With s_i the section of the interphase surrounding a fiber (defined Eq. 7), s_f the developed reactive section of one fiber (defined Eq. 8), $\%S_f$ the initial surface fraction of fibers which is one part of S_u the uncoated surface.

$$s_i = \pi \frac{(D_f + 2 t_i)^2 - D_f^2}{4} \quad \text{Eq. 7}$$

$$s_f = \pi \frac{D_f}{2} \sqrt{\left(\frac{D_f}{2}\right)^2 + l_d^2} \quad \text{Eq. 8}$$

Where D_f is the fibers diameter and t_i the thickness of the interphase.

The resolution of this system of equations allows, in accordance with the oxidation kinetics of the ex-pan fibers, calculating the debonding length (l_d) to fit the mass loss in function of time, for each sample (Figure 14). From a first viewpoint, it appears that the debonding length is much lower when the composite is exposed at 1300°C compared to 1000°C. Although the reactivity of the surfaces, is greater when the temperature increases, a self-healing takes place at 1300°C through the formation of a large quantity of silica, able to form cork against the oxygen diffusion up to the carbon constituents. Moreover, the slight differences obtained between the values of the 2D-RMI and 2D-CVI materials could indicate that the difference in microstructure between the fiber and interphase are negligible on the oxidation kinetics or the quantity of ex-resin carbon from PIP step remains minority (Figure 2).

Finally, since the oxidation rate is relatively constant over time, the debonding length is slightly or not dependent on the exposure time. The slight slowing down at longer times is then linked to a limitation of the oxygen diffusion to the reactive surface, further from the surface of the sample.

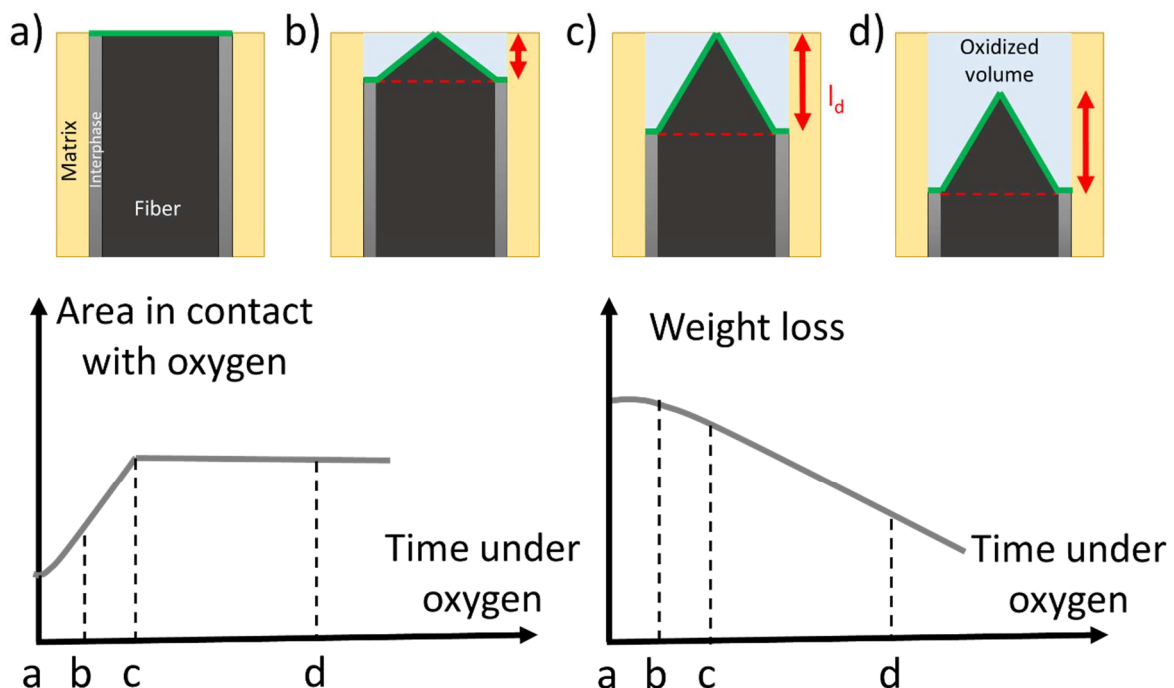


Figure 13. Oxidation scenario considered. a) before oxidation, b) after few seconds, c) after a few tens of seconds and d) after a few tens of minutes.

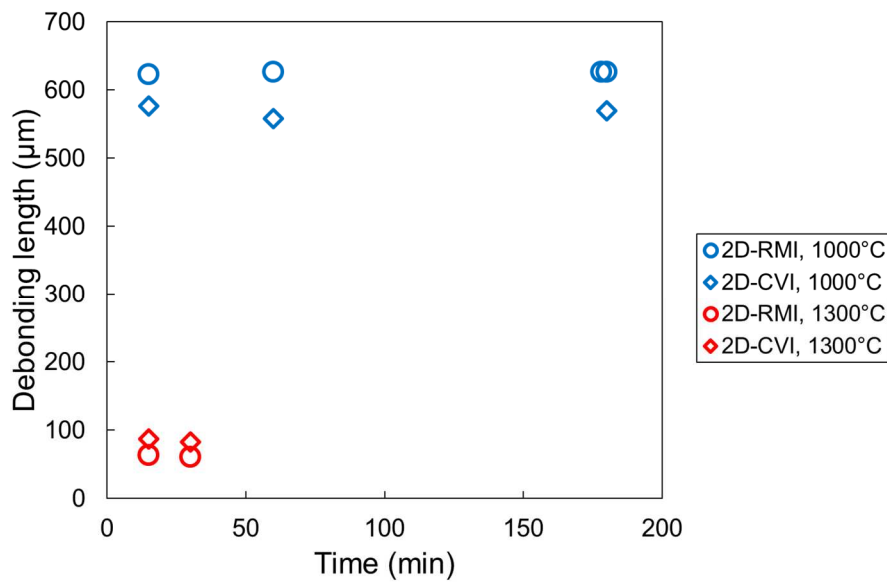


Figure 14. Debonding length calculated to be in accordance with the oxidation kinetics of the ex-pan fibers [39].

(ii) and (iii). The lower increase in kinetics between 1000°C and 1300°C, for 2D-RMI material, could be related to a self healing process on the uncoated surface, with the formation a passivation silica scale. Due to the presence of free silicon in the 2D-RMI composite, the material is more sensitive to reaction with oxygen to form silica. Thus, it was observed on SEM and OM images that the free silicon initially present in the 2D-RMI composite is partially consumed during heat treatment. This silica layer seems to form quickly in the very first moments and it could start to take place as soon as the temperature rises under Argon with the release of oxygen contained in the composite (no mass variation is involved in such a transfer of oxygen inside the composite). The covering power of this silica layer is more effective at higher temperature and for a duration of the holding time. Its passivation role leads to a lowering in the expected oxidation kinetics with temperature in the case of this 2D-RMI composite. However, two facts lead to a similar final length of oxidation propagation between the two composites at 1300°C. Firstly, as mentioned above, access to the interphase and fibers is wider in the case of the 2D-RMI material due to the presence of free carbon inside the tows; its oxidation therefore opens a large diffusion pathway (which leads to a higher debonding length at 1000°C compared to the 2D-CVI material). Secondly, the silica layer observed is extremely thin and brittle (see Figure 8) and therefore does not allow a total coverage of the surface. Finally, at the higher the temperature, a thicker layer of silica is required to provide passivation behavior and the final length of oxidation propagation is similar between these both composites, even if a layer of silica appears more visible on the composite

(iv). Images obtained by tomography show that the monitoring of the oxidation front in the thickness of C/C/SiC composites is feasible at least for 2D-RMI composite. To validate this observation, the oxidized carbon mass can be evaluated from the images obtained in tomography and compared with the values obtained in TGA. The grey level histograms revealed that it is not possible to distinguish the porosities of the oxidized area by performing a simple thresholding. In order to extract the percentage of oxidized surface into each slice, it is therefore assumed that the porosity ratio is constant throughout the sample. Thus, by moving away from the oxidized zone, it is possible to determine this porosity ratio for each sample (%P) (values closed to $1.5\% \pm 0.5\%$ for 2D-RMI composites), from images done on non affected materials. This last value is then subtracted from the percentage of empty area (%Se_i) to define the quantity of oxidized carbon from each slice (%S_i).

$$\%S_i = \%Se_i - \%P \quad \text{Eq. 9}$$

Assuming that mass loss is essentially related to the oxidation of carbon fibers and that the mass gain generated by the creation of silica is negligible, the loss of mass $m_{oxidized}$ is defined as :

$$m_{oxidized} = \rho_{carbon} V_{oxidized} \quad \text{Eq. 10}$$

ρ_{carbon} represents the density of carbon (taken as 1.8 g.cm^{-3}), and $V_{oxidized}$ the oxidized volume defined as :

$$V_{oxidized} = S_u Res \sum_{i=0}^n \%S_i \quad \text{Eq. 11}$$

Where S_u is the surface without coating, Res is the resolution (equal to $4 \mu\text{m}$) and $\%S_i$ is the percentage of oxidized section, calculated from each image (Eq. 9).

These calculated values for 2D-RMI materials are in agreement with the experimental mass losses measured in TGA (Figure 15). However, for the 2D-CVI materials, for long exposure times to oxidation, such a calculated amount of oxidized carbon is much lower than that weighted by TGA.

As previously shown on Figure 9, done with a resolution of $4 \mu\text{m}$, μCT does not allow a sharp distinction between the fibers and the SiC matrix for 2D-CVI material. As a result, the images cannot be well interpreted and the quantification of the volume of carbon performed before and after oxidation is very difficult to carry out. An underestimation of the amount of oxidized material is obtained in more than 50% of the samples, characterized with a deviation higher than twenty times the value. Measurements at a resolution of $2 \mu\text{m}$ have not allowed a better distinction between the

fibers and the matrix. These results confirm the observations made in Figure 9 where the oxidation front is differently pronounced inside both composites, in 3D visualization.

These results show the ability of tomography to separate the different phases inside a composite material (and therefore their change of morphology as during an oxidation). However, the accuracy of this method depends mainly on the size of the volumes of matters with similar or different molecular masses. Indeed, the size of the fibers is the same for both materials, but in the 2D-RMI material, they are surrounded with carbon from the PIP process. Reversely, a larger amount of SiC embeds each fiber of the 2D-CVI material. As a result, voxels containing fibers and matrix have a higher gray level than a voxel containing only fibers. Moreover, on geometric considerations, only one voxel with 4 μm sides can be inserted in a fiber since the length of its diagonal is already close to the diameter of one fiber. Such a situation should be improbable. This ratio is very slightly improved when voxels with 2 μm sides are used (if one voxel always contains carbon, its 8 neighbors should probably be at a C/SiC interface). Consequently, the SiC and C phases cannot be uncorrelated, as reported in Table 2. These difficulties of image analyses remain present once the C phase is oxidized. These results suggest that tomography, at this resolution, is not an effective means for monitoring the oxidation inside all C/C/SiC composites. Higher resolutions are necessary leading to a smaller volume analysed.

For the 2D-RMI composite, the analyses of μCT images are appropriate to extract the position of the oxidation front for different aging temperatures and holding times. These evolutions of the quantity of oxidized carbon deep inside the composite are then compared on Figure 16.

In each aging conditions, the profiles of the percentage of oxidized section appear noisy but remain continuous. These variations have to be related to the changes of stacking inside the fibrous architecture, with variations in fiber contents in successive slices of observation (a similar periodicity around 800-1000 μm can be found in the variations of percentage of oxidized section (Figure 16) and the fibrous architecture (Figures 9-12 and Tables 2-3)).

Profiles of evolution of oxidation fronts in depth are generally similar between the different aging conditions. The position of the decrease of oxidized surface appears later in depth with longer holding times and higher temperatures. A constant value of oxidized surface indicates that all the C phase has been oxidized at this depth. So, the deduced quantity of fibers contained in this material is close to 70%; initially, without aging, the values of carbon have been evaluated close to 80% for some samples (Table 4) and this value remains similar to that proposed in the literature [5], [15]. Again, the working resolution of imaging has a significant influence on the determination of fiber or carbon phase quantities.

The gradient of percentage of oxidized section observed in the depth indicates that the front of oxidation is not flat. Due to the presence of intra-wire and inter-wire porosity, oxidation of the fibers perpendicular to the reactive initial composite surface (the uncoated surface) is not similar in all position in depth. Indeed, the tows are surrounded by SiC matrix, and oxygen has access to the parallel fibers only through the cracks generated during the cooling of the manufacturing process [7], [18]. With the oxidation of these fibers, more oxygen diffusion pathways in a transversal direction can be opened, mainly at each crossing of tows. The continuous development of reactive surfaces contributes to consume a larger part of the diffusing oxygen.

(v). After analysis of the images obtained in tomography and observation of the optical micrographs of the oxidized materials, it was deduced that the oxidation of the carbon fibers and the pyrocarbon interphase occurs mainly where the largest surfaces are in contact with oxygen, in order of importance: the uncoated surface, macropores, mesopores and finally microcracks. Thus, oxidation occurs mainly where the pores are inter-connected and their sizes are sufficiently large to make easier the access of oxygen up the fibers. As a consequence, the inability of tomography to detect microporosities is not a major disadvantage in this case because they have a minor impact on the oxidation processes. Note, however, that if the entire sample is coated, the impact of microcracks could be more significant on the propagation of oxygen within the material and could lead to a less accurate assessment of the oxidized quantity by tomography at this resolution.

Although they occupy a significant volume within composites, the macropores observed by tomography do not seem to play a major role in the distribution of the oxidized zone in composites. In addition, this information confirms that these pores are not connected as suggested by the image analysis done (Table 3).

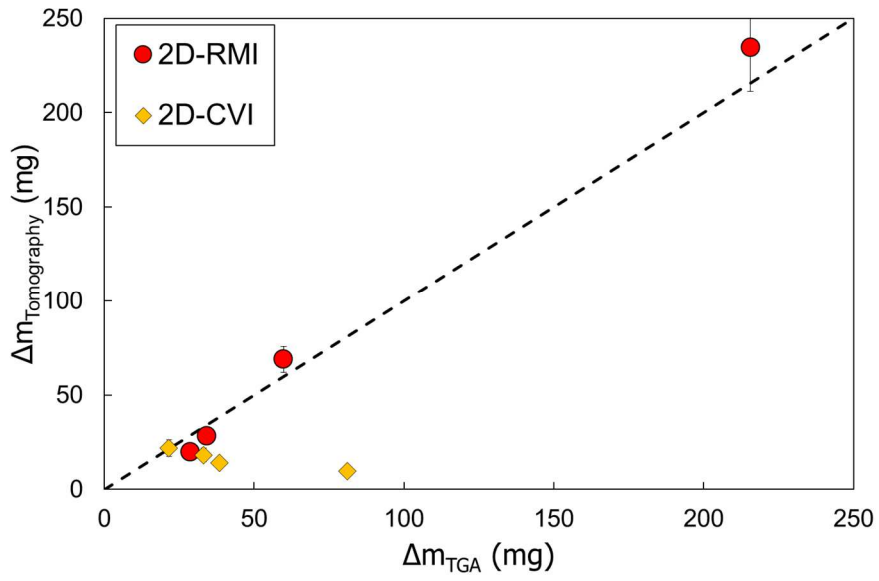


Figure 15. Comparison of the mass loss evaluated by tomography and measured by TGA.

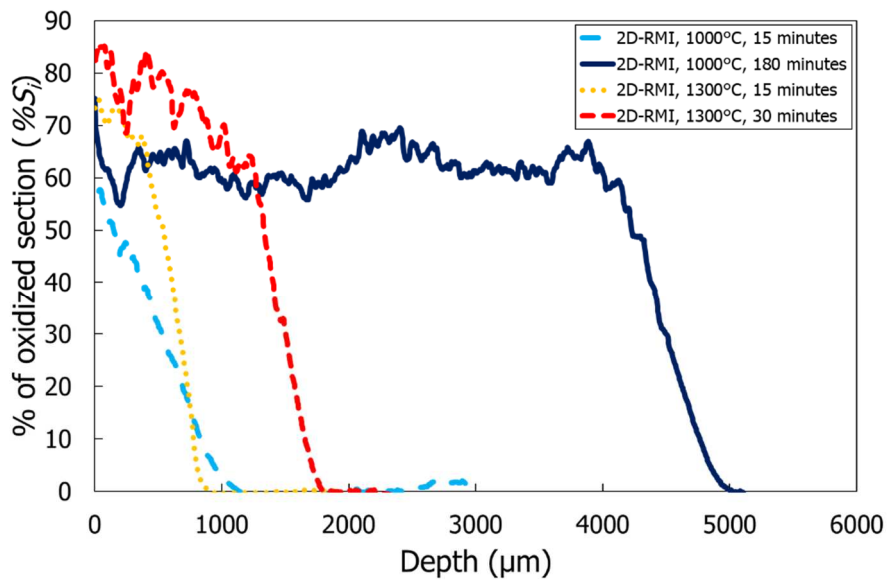


Figure 16. Oxidation profiles in the sample thickness (name of samples: “supplier, T°C, time in minutes”).

5. Conclusion

Several experimental techniques were used to characterize the oxidation of two C/C/SiC composites.

In a first step, an analysis of the unoxidized samples was carried out to evaluate the ability of tomography to determine the composition of the composites. The data were compared with conventional methods. Tomography therefore makes it possible to characterize accurately pores, but only with a size two or three times larger than the selected working resolution. In addition, more data than conventional method are gotten since it is achievable to separate the open and closed pores and to have information on their numbers, their shapes, and their locations inside the materials. It is therefore possible to use this technique to easily visualize the distribution of pores from a mesoscopic to macroscopic scale within C/C/SiC composites

In a second step, tests at 1000°C and 1300°C under air were conducted using the TGA in order to follow the evolution of the oxidation of the composites. Analyses using different characterization techniques such as Xray micro-tomography, scanning electron microscope and optical microscopy were then carried out after the tests. Qualitative and quantitative analyses were performed. The main conclusions are as follows.

Due to their different resolutions, the three characterizations techniques appear to be complementary. μ CT is an appropriate technique to characterize the oxidation of some C/C/SiC composites. However, the quality of the analysis depends on the distribution of carbon fibers in the silicon carbide matrix. In the case where the fibers are particularly surrounded by SiC, the contrast between the phases is insufficient and it is then impossible to characterize the oxidation of these composites at the resolutions used here (4 μ m). Tomography therefore appears to be a promising means of monitoring the oxidation of parts in service.

Moreover, as already observed by several authors, the oxidation of a fiber does not develop in a parallel plan to the section but as conical shape. To calculate the oxidation kinetics related to the surface, it is therefore necessary to take into account the geometry of the fibers that offers a much more important reactive surface. This correction allows being consistent with various works from the literature.

The oxidation kinetics of these materials are quite similar for the two composites and an oxidation front has been observed indicating that oxidation only occurs when the fibers are in close contact with oxygen, in sufficiently large pores. In other words, the micropores observed in mercury intrusion porosity have a relatively limited impact on the transport of oxygen within the composite.

Finally, the differences in oxidation front observed on the two composites 2D-RMI and 2D-CVI appeared mainly related to the presence of free Silicon and of the free Carbon in the matrix of the 2D-RMI composite material. At 1000°C, the access to the interphase and fibers is wider in the case of the 2D-RMI material due to the presence of free carbon inside the tows. Its oxidation therefore opens a large diffusion pathway which leads to a higher debonding length compared to the 2D-CVI material and therefore a sharper oxidation front in the material. At 1300°C, the free silicon transforms into a protective glass phase that is clearly visible at the SEM and induces a decrease in the oxidation rate for this composite. However, this silica layer is too thin to fully protect the 2D-RMI material leading to similar debonding lengths in both composites.

6. Acknowledgements

This work has been supported by the Centre National de Recherche Scientifique (CNRS) and the Commissariat à l'énergie atomique et aux énergies alternative (CEA). The authors are grateful to Alexandre Allemand, Patrick David and Christophe Tallaron (CEA) for valuable insights and Laurine Lapuyade and Olivier Antonin (LCTS) for their technical support.

7. References

- [1] R. Naslain, « Design, preparation and properties of non-oxide CMCs for application in engines and nuclear reactors: an overview », *Compos. Sci. Technol.*, vol. 64, n° 2, p. 155-170, févr. 2004, doi: 10.1016/S0266-3538(03)00230-6.
- [2] J. Nie, Y. Xu, L. Zhang, L. Cheng, et J. Ma, « Microstructure and tensile behavior of multiply needled C/SiC composite fabricated by chemical vapor infiltration », *J. Mater. Process. Technol.*, vol. 209, n° 1, p. 572-576, janv. 2009, doi: 10.1016/j.jmatprotec.2008.02.035.
- [3] B. Heidenreich, « C/SiC and C/C-SiC Composites », in *Ceramic Matrix Composites*, Wiley-Blackwell, 2014, p. 147-216.
- [4] M. Balat-Pichelin, L. Charpentier, F. Panerai, O. Chazot, B. Helber, et K. Nickel, « Passive/active oxidation transition for CMC structural materials designed for the IXV vehicle re-entry phase », *J. Eur. Ceram. Soc.*, vol. 2, n° 35, p. 487-502, 2015, doi: 10.1016/j.jeurceramsoc.2014.09.026.
- [5] S. Fan *et al.*, « Progress of ceramic matrix composites brake materials for aircraft application », vol. 44, p. 313-325, janv. 2016.
- [6] G. Camus et J. E. Barbier, « Tensile behavior of a 2D woven C/SiC composite at ambient and elevated temperatures », *Am. Ceram. Soc.*, déc. 1995.
- [7] F. Lamouroux, G. Camus, et J. Thébault, « Kinetics and Mechanisms of Oxidation of 2D Woven C/SiC Composites: I, Experimental Approach », *J. Am. Ceram. Soc.*, vol. 77, n° 8, p. 2049-2057, août 1994, doi: 10.1111/j.1151-2916.1994.tb07096.x.
- [8] F. Lamouroux et G. Camus, « Oxidation effects on the mechanical properties of 2D woven C/SiC composites », *J. Eur. Ceram. Soc.*, vol. 14, n° 2, p. 177-188, janv. 1994, doi: 10.1016/0955-2219(94)90105-8.
- [9] M. Halbig et A. Eckel, « Oxidation of Continuous Carbon Fibers Within a Silicon Carbide Matrix Under Stressed and Unstressed Conditions », août 2000.
- [10] S. Singh, V. Singh, S. Kumari, A. Udayakumar, et V. V. Bhanu Prasad, « Microstructural-property correlation of CVI processed Cf/SiC composites and property enhancement as a function of CVD SiC seal coating », *Ceram. Int.*, vol. 41, n° 10, Part B, p. 14896-14907, déc. 2015, doi: 10.1016/j.ceramint.2015.08.020.

- [11] C.-P. Yang, L. Zhang, B. Wang, T. Huang, et G.-Q. Jiao, « Tensile behavior of 2D-C/SiC composites at elevated temperatures: Experiment and modeling », *J. Eur. Ceram. Soc.*, vol. 37, n° 4, p. 1281-1290, avr. 2017, doi: 10.1016/j.jeurceramsoc.2016.11.011.
- [12] S. Singh, V. Singh, S. Kumari, A. Udayakumar, et V. V. B. Prasad, « A comparative study of tensile strength of Cf/SiC composites having single layer and multilayer interphases », *Ceram. Int.*, juill. 2019, doi: 10.1016/j.ceramint.2019.07.099.
- [13] W. Krenkel, « Cost Effective Processing of Cmc Composites by Melt Infiltration (Lsi-Process) », in *25th Annual Conference on Composites, Advanced Ceramics, Materials, and Structures: A: Ceramic Engineering and Science Proceedings*, M. Singh et T. Jessen, Éd. John Wiley & Sons, Inc., 2001, p. 443-454.
- [14] R. Kochendörfer et N. Lützenburger, « Applications of CMCs Made via the Liquid Silicon Infiltration (LSI) Technique », in *High Temperature Ceramic Matrix Composites*, W. Krenkel, R. Naslain, et H. Schneider, Éd. Wiley-VCH Verlag GmbH & Co. KGaA, 2001, p. 275-287.
- [15] W. Krenkel et N. Langhof, « Ceramic Matrix Composites for High Performance Friction Applications », in *Proceedings of the IV Advanced Ceramics and Applications Conference*, Atlantis Press, Paris, 2017, p. 13-28.
- [16] G. Camus, L. Guillaumat, et S. Baste, « Development of damage in a 2D woven C/SiC composite under mechanical loading: I. Mechanical characterization », *Compos. Sci. Technol.*, vol. 56, n° 12, p. 1363-1372, janv. 1996, doi: 10.1016/S0266-3538(96)00094-2.
- [17] Y. Xu, P. Zhang, H. Lu, et W. Zhang, « Numerical modeling of oxidized C/SiC microcomposite in air oxidizing environments below 800°C: Microstructure and mechanical behavior », *J. Eur. Ceram. Soc.*, vol. 35, n° 13, p. 3401-3409, nov. 2015, doi: 10.1016/j.jeurceramsoc.2015.05.039.
- [18] M. C. Halbig, J. D. McGuffin-Cawley, A. J. Eckel, et D. N. Brewer, « Oxidation Kinetics and Stress Effects for the Oxidation of Continuous Carbon Fibers within a Microcracked C/SiC Ceramic Matrix Composite », *J. Am. Ceram. Soc.*, vol. 91, n° 2, p. 519-526, févr. 2008, doi: 10.1111/j.1551-2916.2007.02170.x.
- [19] I. W. Smith, « The intrinsic reactivity of carbons to oxygen », *Fuel*, vol. 57, n° 7, p. 409-414, juill. 1978, doi: 10.1016/0016-2361(78)90055-8.

- [20] F. Lamouroux, R. Naslain, et J.-M. Jouin, « Kinetics and Mechanisms of Oxidation of 2D Woven C/SiC Composites: II, Theoretical Approach », *J. Am. Ceram. Soc.*, vol. 77, n° 8, p. 2058-2068, août 1994, doi: 10.1111/j.1151-2916.1994.tb07097.x.
- [21] R. Naslain *et al.*, « Oxidation mechanisms and kinetics of SiC-matrix composites and their constituents », *J. Mater. Sci.*, vol. 39, n° 24, p. 7303-7316, déc. 2004, doi: 10.1023/B:JMSC.0000048745.18938.d5.
- [22] P. Crocker et B. McEnaney, « Oxidation and fracture of a woven 2D carbon-carbon composite », *Carbon*, vol. 29, n° 7, p. 881-885, janv. 1991, doi: 10.1016/0008-6223(91)90163-D.
- [23] W. H. Glime et J. D. Cawley, « Oxidation of carbon fibers and films in ceramic matrix composites: A weak link process », *Carbon*, vol. 33, n° 8, p. 1053-1060, janv. 1995, doi: 10.1016/0008-6223(95)00034-B.
- [24] F. Lamouroux, X. Bourrat, R. Naslain, et J. Sevely, « Structure/oxidation behavior relationship in the carbonaceous constituents of 2D-C/PyC/SiC composites », *Carbon*, vol. 31, n° 8, p. 1273-1288, janv. 1993, doi: 10.1016/0008-6223(93)90086-P.
- [25] N. S. Jacobson et D. M. Curry, « Oxidation microstructure studies of reinforced carbon/carbon », *Carbon*, vol. 44, n° 7, p. 1142-1150, juin 2006, doi: 10.1016/j.carbon.2005.11.013.
- [26] L. Filipuzzi, G. Camus, R. Naslain, et J. Thebault, « Oxidation Mechanisms and Kinetics of 1D-SiC/C/SiC Composite Materials: I, An Experimental Approach », *J. Am. Ceram. Soc.*, vol. 77, n° 2, p. 459-466, févr. 1994, doi: 10.1111/j.1151-2916.1994.tb07015.x.
- [27] F. Wan, R. Liu, Y. Wang, Y. Cao, C. Zhang, et T. J. Marrow, « Damage development during flexural loading of a 5-directional braided C/C-SiC composite, characterized by X-ray tomography and digital volume correlation », *Ceram. Int.*, vol. 45, n° 5, p. 5601-5612, avr. 2019, doi: 10.1016/j.ceramint.2018.12.020.
- [28] J. Beckmann, M. Finn, S. Glaubitz, U. Mücke, et G. Weidemann, « Damage Characterization of C/C-SiC-Ceramics », in *High Temperature Ceramic Matrix Composites*, W. Krenkel, R. Naslain, et H. Schneider, Éd. Weinheim, FRG: Wiley-VCH Verlag GmbH & Co. KGaA, 2006, p. 511-516.
- [29] J. M. Hausherr, W. Krenkel, F. Fischer, et V. Altstädt, « Nondestructive Characterization of High-Performance C/SiC-Ceramics Using X-Ray-Computed Tomography: Characterization of C/SiC-Ceramics Using X-Ray CT », *Int. J. Appl. Ceram. Technol.*, vol. 7, n° 3, p. 361-368, nov. 2009, doi: 10.1111/j.1744-7402.2009.02449.x.

- [30] F. Wan, T. J. Pirzada, R. Liu, Y. Wang, C. Zhang, et T. J. Marrow, « Microstructure Characterization by X-Ray Computed Tomography of C/C-SiC Ceramic Composites Fabricated with Different Carbon Fiber Architectures », *Appl. Compos. Mater.*, vol. 26, n° 4, p. 1247-1260, août 2019, doi: 10.1007/s10443-019-09778-2.
- [31] V. Srivastava, « Micro-Structural Characterization of Si-SiC Ceramic Derived from C/C-SiC Composite », *Am. J. Mater. Sci.*, vol. 2, p. 1-4, févr. 2012, doi: 10.5923/j.materials.20120201.01.
- [32] A. P. Gillard, G. Couégnat, O. Caty, A. Allemand, P. Weisbecker, et G. Vignoles, « A quantitative, space-resolved method for optical anisotropy estimation in bulk carbons », *Carbon*, vol. 91, p. 423-435, sept. 2015, doi: 10.1016/j.carbon.2015.05.005.
- [33] E. W. Washburn, « The Dynamics of Capillary Flow », *Phys. Rev.*, vol. 17, n° 3, p. 273-283, mars 1921, doi: 10.1103/PhysRev.17.273.
- [34] S. R. Stock, « X-ray microtomography of materials », *Int. Mater. Rev.*, vol. 44, n° 4, p. 141-164, avr. 1999, doi: 10.1179/095066099101528261.
- [35] S. R. Stock, « Recent advances in X-ray microtomography applied to materials », *Int. Mater. Rev.*, vol. 53, n° 3, p. 129-181, mai 2008, doi: 10.1179/174328008X277803.
- [36] E. Maire et P. J. Withers, « Quantitative X-ray tomography », *Int. Mater. Rev.*, vol. 59, n° 1, p. 1-43, janv. 2014, doi: 10.1179/1743280413Y.0000000023.
- [37] FEI Visual Sciences Group, « Visual Sciences Group, 2009. Avizo User's Guide Version 6. » .
- [38] G. Vignoles, P. Weisbecker, J.-M. Leyssale, S. Jouannigot, et G. Chollon, « Carbones pyrolytiques ou pyrocarbones : des matériaux multiéchelles et multiperformances », p. 25, 2015.
- [39] M. Zancanaro, N. Bertrand, et F. Rebillat, « Definition of Optimized Conditions to Extract Accurate Kinetic Laws from TGA Experiments: Modeling and Validation », *Oxid. Met.*, vol. 87, n° 3, p. 393-402, avr. 2017, doi: 10.1007/s11085-017-9716-6.
- [40] H. Marsh et K. Kuo, « Chapter 4 - Kinetics and Catalysis of Carbon Gasification », in *Introduction to Carbon Science*, H. Marsh, I. A. S. Edwards, R. Menendez, B. Rand, S. West, A. J. Hosty, K. Kuo, B. McEnaney, T. Mays, D. J. Johnson, J. W. Patrick, D. E. Clarke, J. C. Crelling, et R. J. Gray, Éd. Butterworth-Heinemann, 1989, p. 107-151.
- [41] X. Bertran, « Comportement en milieu oxydant d'un composite carbone/carbone pour applications structurales entre 150 et 400°C dans l'aéronautique civile », UNIVERSITÉ BORDEAUX 1, 2014.

Figure 1. Sample used for TGA measurements.	5
Figure 2. Comparisons of polarized light images of the two materials.	6
Figure 3. In left, results from the mercury porosimetry; incremental intrusion pore (straight lines) and cumulative intrusion (dot lines) versus equivalent pore diameter for the two composites. In right, results from tomography images, volume fraction of pore (straight lines) and number fraction of pores (dot lines); versus equivalent pore diameter for the two composites (voxel resolution = 8 μm).8	8
Figure 4. Sphericity of pores distribution for the two composites obtained by tomography analyses.	11
Figure 5. Evolution of the weight loss related to the uncoated section S_u as a function of time. .	12
Figure 6. Comparison of composite oxidation kinetics with an ex-pan and cellulose fiber model [39].	12
Figure 7. Developed oxidized surfaces obtained after thermal treatments at 1000 and 1300°C, SEM images obtained in secondary electrons.	14
Figure 8. SEM micrograph of the surface of and 2D-RMI sample covered by a SiO_2 glass phase after treatment at 30 minutes at 1300°C.	14
Figure 9. Comparison of the resolution obtained by optical microscopy (a,b) and tomography (c,d) for the two materials 2D-RMI (a,c) and 2D-CVI (b,d).	15
Figure 10. Observations by optical microscopy of samples aged at 1300°C for 15 minutes, a) 2D-RMI and b) 2D-CVI, (The uncoated is located at the bottom of images).	15
Figure 11. Tomography images of both composites after an ageing treatment at 1300°C for 15 minutes in dry air.	17
Figure 12. Processing carried out on images obtained by tomography on a 2D-RMI sample after ageing treatment at 1000°C for 15 minutes in dry air; a) Non-thresholded image, b) thersholded image (in black, porosity and oxidized carbon).....	17
Figure 13. Oxidation scenario considered. a) before oxidation, b) after few seconds, c) after a few tens of seconds and d) after a few tens of minutes.....	23
Figure 14. Debonding length calculated to be in accordance with the oxidation kinetics of the ex-pan fibers [39].	24
Figure 15. Comparison of the mass loss evaluated by tomography and measured by TGA.	28
Figure 16. Oxidation profiles in the sample thickness (name of samples: “supplier, T°C, time in minutes”)......	28
Table 1. Summary table of the microstructural properties of the two C/SiC composites: 2D-RMI and 2D-CVI.....	7
Table 2. Tomography of the microstructures as received at a resolution of 8 μm : 3D visualization and typical histogram of grey levels obtained for the two materials.	10
Table 3. Distribution of pores in the two composites from the tomography. For quantification, pores are labeled, colors correspond to pore labels.....	20
Table 4. Volume fractions and density values extracted from tomography images. Data not available for 2D-CVI material due to inability to clearly distinguish fibers and matrix with threshold image treatment.....	20